Nuclear Instruments and Methods in Physics Research A 392 (1997) 324–329

NUCLEAR INSTRUMENTS & METHODS IN PHYSICS RESEARCH Section A

ELSEVIER

Gamma and beta intra-operative imaging probes

Edward J. Hoffman[a,*], Martin P. Tornai[a], Craig S. Levin[a], Lawrence R. MacDonald[b], Stefan Siegel[a,c]

[a]*Division of Nuclear Medicine & Biophysics, UCLA School of Medicine, Los Angeles, CA 90095, USA*
[b]*Department of Physics, UCLA, Los Angeles, CA 90095, USA*
[c]*Department of Nuclear Medicine, National Institutes of Health, Bethesda, MD 20892, USA*

Abstract

Small area ($\sim$1.5 cm^2) scintillation cameras for imaging gammas and betas using inter-changeable detector front ends were built and characterized. Components common to both emission imaging cameras include: (1) fiber optic bundles 2–3 m long, comprised of multi-clad fibers which connect the scintillation detector to (2) an MC-PMT; (3) parallel MC-PMT outputs feed a resistive positioning network and i–V converter/line driver network which produce balanced ^+X, ^-X, ^+Y, and ^-Y outputs; and (4) four ADCs and a Macintosh PC for system control and image display. The beta and gamma devices used distinct scintillation detectors which were characterized by both simulation and measurement.

The beta camera utilized a 0.5 mm by 1.25 cm ϕ CaF_2(Eu) scintillation crystal coupled, through a diffusing light guide, to 19 2-mm ϕ optical fibers. These front-end fibers are in turn coupled by a more flexible fiber bundle to the MC-PMT. CaF_2(Eu) has high light output, high beta sensitivity, and low gamma sensitivity. Image signals are histogrammed and displayed after Anger logic computations are performed on digitized signals. The beta camera has $<$0.6 mm FWHM intrinsic resolution.

The gamma camera concept was tested with matrices of discrete 1×1 mm^2 and 2×2 mm^2 CsI(Tl) and NaI(Tl) crystals of various lengths, and 3 mm thick continuous crystals. Configurations using 4×4 element matrices with one-to-one coupling between crystals and fiber channels, and light diffusers between each crystal matrix and fibers were evaluated. The continuous crystals were coupled directly to the fiber optics with signal and data processing analogous to the beta camera. Coupling of discrete crystals to fiber optics by both methods gave essentially perfect identification of the crystal of interaction, allowing spatial resolution to be defined by the crystal size and collimator. The continuous crystal gamma camera gave intrinsic resolution of $\sim$1.4 mm FWHM.

1. Introduction

Intra-operative imaging probes are designed to be used by neurosurgeons to locate residual radiolabeled tumor after the bulk of tumor has been excised. Before neurosurgery, patients are injected with beta or gamma emitting radiopharmaceuticals, the primary mass of tumor is removed, and the neurosurgeon uses the imaging probe to locate labeled tumor remnants.

We designed, built and characterized a beta sensitive imaging probe for use in the brain [1–6]. The intra-operative probe utilized a 0.5 mm by 1.25 cm ϕ CaF_2(Eu) crystal coupled through a light diffuser to 19 hexagonally arranged, 2 mm ϕ front-end fiber optics [5]. This front end was coupled to longer 0.925 mm ϕ bundles of fibers, which guided the light to a parallel output multi-channel photomultiplier (MC-PMT). After charge division multiplexing, appropriate shaping and digitization, the signals were combined to form an image. The beta imaging intra-operative probe had 0.53 ± 0.07 mm FWHM intrinsic spatial resolution. The beta imaging system is extended to gamma imaging in this work. The CaF_2(Eu) crystal is replaced by gamma sensitive arrays of CsI(Tl) or NaI(Tl) crystals and/or a single continuous CSI(Tl) crystal.

Intra-operative gamma imaging detectors have been reported utilizing intrinsic CdTe [7,8] and HgI_2 [9,10] semiconductor detectors. A system for high resolution gamma ray imaging is also being developed with CSI(Tl) scintillators and HgI_2 photodetectors [11]. Advantages of our fiber optic system include: the insulating effects of fiber optics which remove all voltage and current sources from the surgical cavity; simple adaptability to allow

* Corresponding author. Tel.: + 1 310 825 8851; fax: + 1 310 825 4517; e-mail: ehoffman @ mail.nuc.ucla.edu.

PII S0168-9002(97)00247-7

detection of both beta and gamma radiation; and the system fits easily into small openings and can produce images of clinical value [2,3,5].

2. Experimental methods

2.1. Detector simulations

Although continuous crystals were also tested, it was apparent that matrices of small crystals would provide the solution for the gamma imaging probe. For these small crystals it is essential that the gamma-ray (~140 keV) be totally absorbed in the crystal volume, and that the light emitted from the end of the crystal be adequate for crystal identification and energy thresholding. A multiple interaction Monte Carlo code [12] was utilized to determine the efficiencies, and energy deposited in small parallel-piped crystals varying in size from $1 \times 1\,mm^2$ to $3 \times 3\,mm^2$, and lengths from 2 to 10 mm. An optical tracking Monte Carlo [13], utilizing the ΔX, ΔY, ΔZ position information from the gamma interaction Monte Carlo, was used to estimate the light output from the various geometries.

2.2. Imaging probe components

The gamma imaging probe utilizes common elements in the imaging chain which were investigated and optimized for use in the beta imaging probes [5]. The common components include: (1) 15 cm long fiber optic bundles (which will be extended to 2–3 m), comprised of multi-clad fibers which connect the scintillation detector to a (2) Philips XP1722 64-channel MC-PMT; (3) parallel MC-PMT outputs which feed a gain balancing, resistive charge positioning network and i–V converter/line driver network producing ^{+}X, ^{-}X, ^{+}Y, and ^{-}Y outputs; and (4) various NIM shaping and discriminating modules, CAMAC ADCs for each analog signal, and a Macintosh IIfx for system control and image display.

2.3. Scintillation imaging detectors and optical coupling

The gamma camera concept was tested with available matrices of discrete $1 \times 1\,mm^2$ and $2 \times 2\,mm^2$ CsI(Tl) and NaI(Tl) crystals with 1.25 and 2.5 mm pitch, respectively, and lengths ranging from 2.5 to 6 mm. In addition, a 3 mm thick by $14 \times 14\,mm^2$ continuous CsI(Tl) crystal was tested. Although CsI(Tl) has ~65% higher stopping power at 140 keV and also produces ~35% more light than NaI(Tl), its maximum emission wavelength ($\lambda_{max} = 530$ nm) is not well matched to bialkali photocathode PMTs, giving a signal amplitude of about 50% of NaI(Tl).

The detector-end of the experimental configurations are illustrated in Fig. 1, left. With 4×4 element matrices

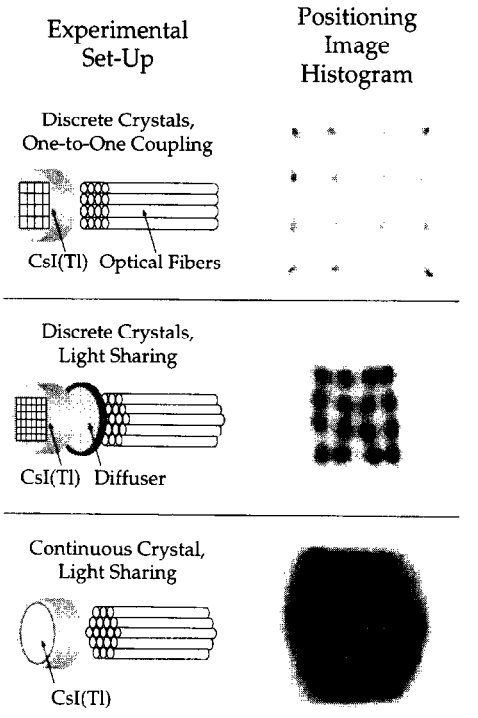

Fig. 1. (Left) Conceptual diagrams of the experimental configurations of the gamma imaging probes' front-ends and (right) the corresponding flood field positioning image histograms for the $1 \times 1 \times 4\,mm^3$ discrete crystal 4×4 element array without and with light diffuser, and the $14 \times 14 \times 3\,mm^3$ continuous crystal irradiated with ^{57}Co. Middle figure illustrates that one-to-one coupling is not necessary when light sharing is employed.

of crystals, one-to-one coupling between crystals and MC-PMT channels was evaluated with arrays of 0.925 mm ϕ and 2 mm ϕ multi-clad optical fibers connected to each of the $1 \times 1\,mm^2$ and $2 \times 2\,mm^2$ crystal arrays. Configurations using light diffusers between each detector matrix and 19 hexagonally arranged 2 mm ϕ optical fibers, analogous to the beta imaging probe [2,5], were also evaluated. The continuous crystal was coupled directly to the fiber optics without the use of a light diffuser. All data were collected in list mode to allow retrospective processing. To form an image the ^{+}X, ^{-}X, ^{+}Y, and ^{-}Y outputs were processed with the following equations:

$$X = \frac{^{+}X - {}^{-}X}{^{+}X + {}^{-}X} \quad \text{and} \quad Y = \frac{^{+}Y - {}^{-}Y}{^{+}Y + {}^{-}Y}. \tag{1}$$

Since their positioning signals are independent of each other [14], the one-to-one coupled arrays require no gain balancing. However, the discrete/diffuser and continuous crystal detectors use individual gain balancing resistive dividers to minimize spatial non-linearities and gain variations [5].

2.4. Resolution and imaging measurements

The line spread function (LSF) was measured by stepping a 0.3 mm Pb collimated slit of ^{57}Co (122 keV) in 0.2 mm increments across the faces of the detectors. Imaging results were also obtained with a Pb transmission phantom with 1.0 mm holes in the shape of a "stick figure". The transmission phantom was also subsampled at half detector spacings for higher resolution images. In addition, linear interpolation was performed on images from discrete arrays to reduce pixellation effects. Because the phantom did not fit in the field of view (FOV) of either configuration, multiple images were acquired and digitally spliced. All images were normalized by energy windowed flood field responses.

3. Experimental results

3.1. Monte Carlo simulations

The results of the simulations indicate that even 1 mm × 1 mm CsI(Tl) crystals have a high detection efficiency at ~140 keV, provided the crystal is >6 mm deep (Fig. 2(A)). This is significant because CsI(Tl) has approximately 65% greater stopping power at 140 keV than NaI(Tl), which has been the detector of choice. Additional length provides only a modest improvement in sensitivity. Optical tracking simulations in crystals with optimized surface treatment (Fig. 2(B)) indicate improvement in light collection with larger detector areas, and degradation of light collection with greater length, consistent with earlier work [15, 16]. However, larger cross-sectional areas provide only slightly higher yields of scintillation photons for areas larger than 1 mm^2 (Fig. 2(B)), but at the cost of worse spatial resolution.

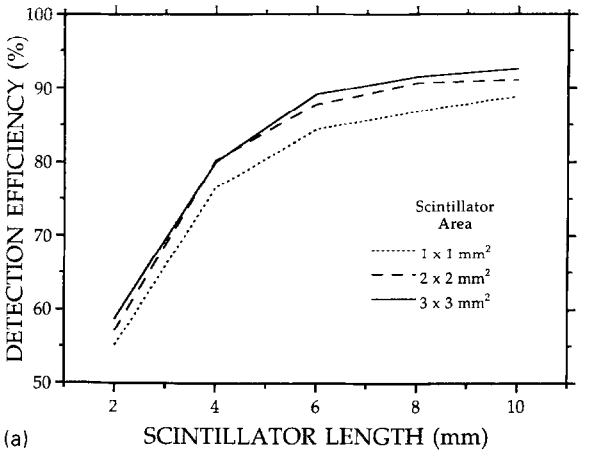

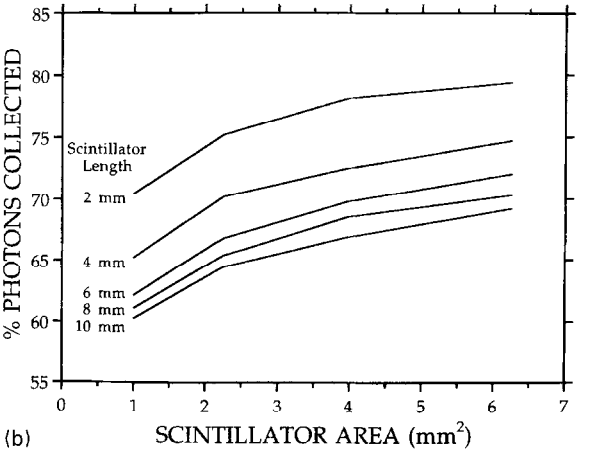

Fig. 2. (a) Monte Carlo simulation results for detection efficiency for 122 keV photons in small parallel-piped CsI(Tl) scintillators. (b) Optical tracking simulation results for small CsI(Tl) crystals directly on a photodetector with unity detection efficiency.

3.2. Positioning image histograms

Images of the detector identifying data for the various detector/fiber coupling schemes are shown in Fig. 1, right. For both cases with 1 × 1 mm^2 CsI(Tl) elements, each element is clearly resolved. With the one-to-one crystal-fiber coupling (Fig. 1, top), the positioning histogram image can obviously accommodate more smaller crystals in its array. Additional crystals can easily be decoded by changing the values in the resistive divider network to accommodate these elements [14].

The thickness of the light diffuser must be optimized (Fig. 3) before a crystal matrix with light diffuser can be used as an imaging device (Fig. 1, middle). For very thin diffusers, the spots corresponding to each crystal are not resolved, they do not even approximate the light distribution expected from a square matrix, and the intensities of the spots vary significantly. As the diffuser thickness is increased from 0.48 to 2.90 mm, the distortion and nonuniformity is greatly reduced with a loss in pulse height of 28%. A thickness of 1.9 mm was chosen as a best compromise of pulse height, resolution uniformity, and sensitivity uniformity. Thus, the image is of the light from each element, and when an event falls into the region corresponding to an element, that event is assigned to that element.

The continuous crystal flood irradiation response (Fig. 1, bottom) is used as a uniformity correction for images acquired with this technique. Sensitivity and gain variations are normalized by this flood image and thresholds are set from the pulse height of the combined signals [5].

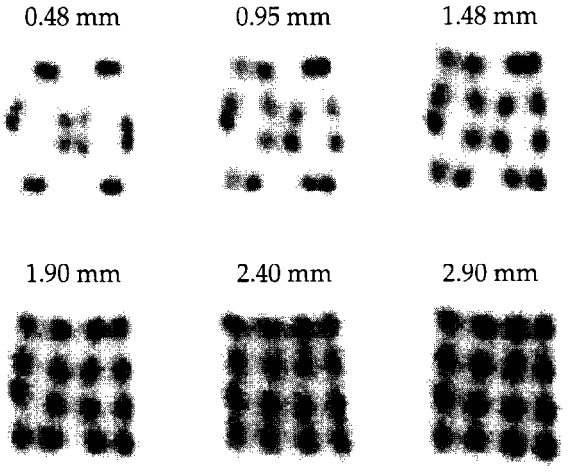

Fig. 3. Flood field image histograms of the 4×4 element $1 \times 1 \times 14\,mm^3$ CsI(Tl) crystals coupled through various thickness light diffusers to the 19 element hexagonal fiber array.

3.3. Detector spectral responses

Prior to imaging with the discrete gamma imaging probe, the image of the crystal array is used to create a position look-up table, similar in principle to that used with PET "block" detectors [17]. Every pixel in the region of the image corresponding to a crystal in the array is assigned the crystal number (Fig. 4(A)), areas not assigned are set to zero, and the resultant matrix forms a lookup table. When an image is taken each event provides an X and Y address for the lookup table, which returns the crystal number when addressed. The energy response for each crystal is also stored (Fig. 4(B)) and used for thresholding each event. This method is used for both the one-to-one and diffuser coupled crystal arrays.

For the diffuser coupled arrays, the variation in pulse height for individual $1 \times 1 \times 2.5\,mm^3$, $1 \times 1 \times 4\,mm^3$, and $2 \times 2 \times 4\,mm^3$ CsI(Tl) crystals was $\pm$ 7.6%, $\pm$ 7.9%, and $\pm$ 11.7%, respectively. The FWHM energy resolutions for all elements at 122 keV were 57.6% $\pm$ 1.8%, 57.4% $\pm$ 2.3%, and 55.8% $\pm$ 3.0% for the CsI(Tl) arrays, respectively, with very clearly defined photopeaks (Fig. 4(B)). With direct one-to-one coupling, these values were similar. A 4×4 element NaI(Tl) array with $2 \times 2 \times 6\,mm^3$ crystals had greater pulse height variability ($\pm$20.9%) and worse energy resolution (60.4% $\pm$2.6%) most likely due to the longer length of the crystals (cf. Fig. 2(B)) and poorer optical coupling due to a 3 mm thick glass window between the crystals and fibers.

The pulse height with the continuous CsI(Tl) crystal was approximately a factor of 3 lower than for the discrete arrays. The differential uniformity of the 3 mm thick crystal flood image was $\pm$ 18% in count variation.

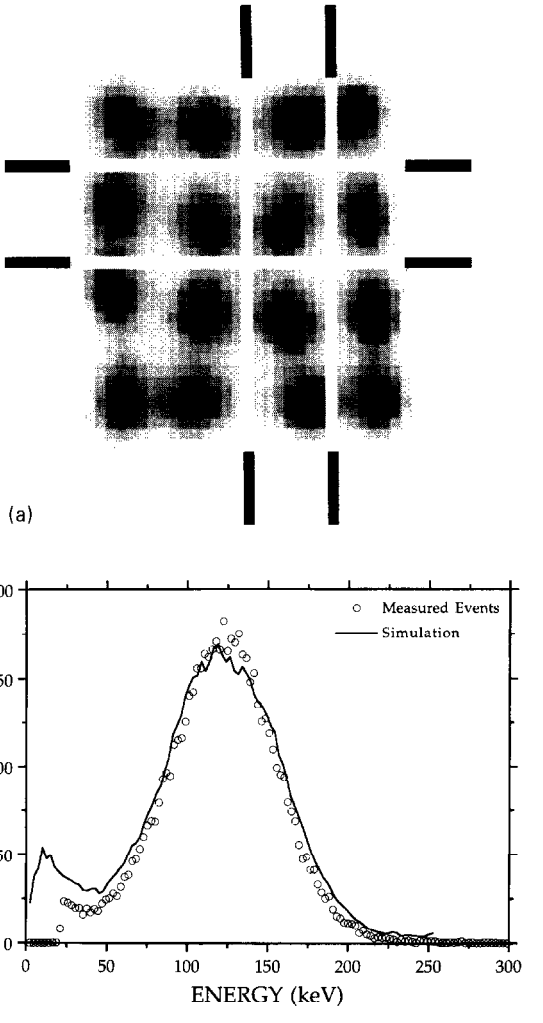

Fig. 4. (a) Flood field image histogram of the $1 \times 1 \times 4\,mm^3$ CsI(Tl) crystals with diffuser and digital crystal identification window. (b) Measured energy response of the windowed crystal in (a) superimposed with Monte Carlo simulation results.

3.4. Resolution and imaging measurements

All of the CsI(Tl) and NaI(Tl) crystal elements in the arrays were well resolved with the one-to-one or diffuser coupled methods (Fig. 1) indicating that the intrinsic spatial resolution will correspond to the crystal size. The LSF of all the diffuser coupled $1 \times 1 \times 4\,mm^3$ CsI(Tl) crystals was 0.92 ± 0.03 mm FWHM (Fig. 5(A)) from Gaussian fits to the data. The LSF for the $14 \times 14 \times 3\,mm^3$ CsI(Tl) crystal was 1.37 ± 0.19 mm and 1.45 ± 0.22 mm FWHM in the X and Y dimensions (Fig. 5(B)), respectively. With intrinsic detector resolution values between 0.9 and 1.5 mm, the collimator will ultimately limit spatial resolution.

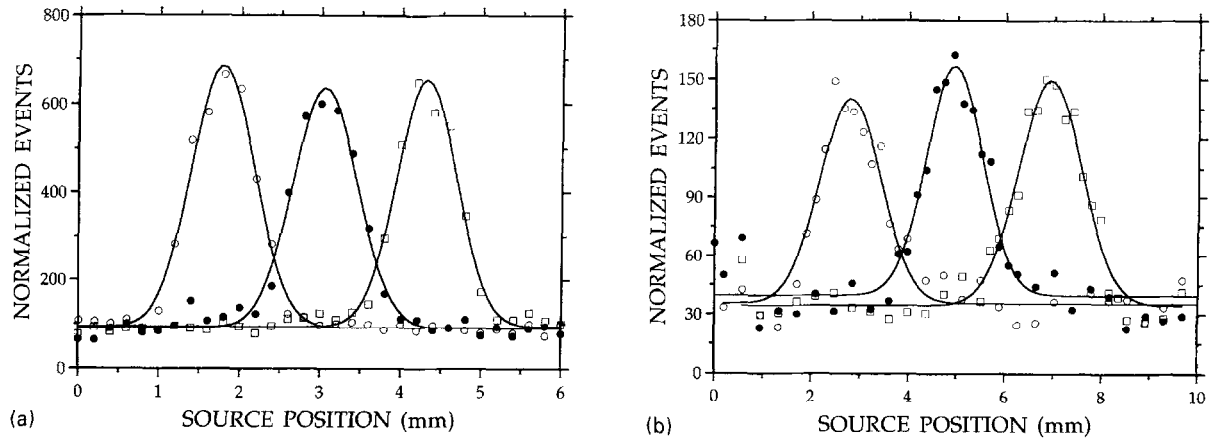

Fig. 5. (a) LSF of three $1 \times 1 \times 4$ mm^3 CsI(Tl) crystals. (b) LSF of the $14 \times 14 \times 3$ mm^3 continuous CsI(Tl) crystal in the X direction. All curves are fit with Gaussians to the measured data.

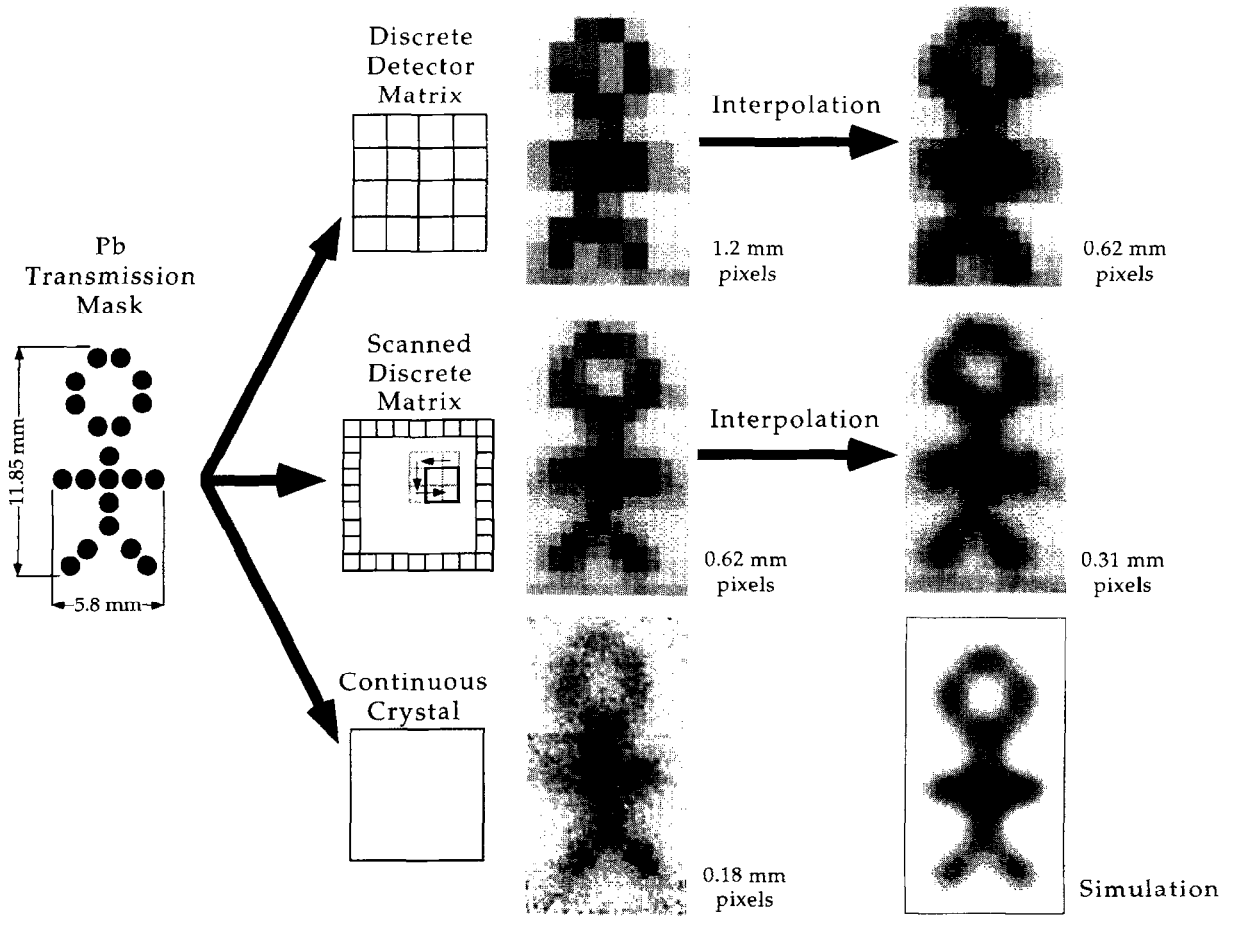

Fig. 6. (Left) Pb transmission phantom with 1 mm ϕ holes spaced on $\sim$1.2 mm vertical and horizontal pitch. (Middle) Results of image acquisition with a single position of the $1 \times 1 \times 4$ mm^3 CsI(Tl) crystal 4×4 element discrete array (top), half-detector spaced acquisition with the same discrete array (middle), and continuous crystal acquisition (bottom). (Right) Simple linear interpolation of the discrete array acquisitions, and Gaussian blurred digital transmission phantom compared to the continuous crystal acquisition.

Images of the stick figure transmission phantom were made with the $1 \times 1 \times 4\,mm^3$ crystal arrays and the continuous CsI(Tl) crystals (Fig. 6). In addition, a continuous image simulation was made of the digital transmission phantom, blurred with a 2D Gaussian filter ($\sigma =$ 0.6 mm) (Fig. 6, lower right). The discrete detector's response reproduces the activity distribution, and the simulated and measured continuous image show excellent correspondence.

4. Conclusions

We have designed, built and characterized a small area, high resolution, fiber optic based detection system for intra-operative imaging [1–6]. In this work we described the extension of the original beta imaging system to include gamma imaging. The CsI(Tl) detector systems were shown to have excellent intrinsic spatial resolution and sensitivity for $\sim$140 keV gammas in both the simulations and the measurements. It is anticipated that CsI(Na), which has essentially the same stopping power, effective Z, and density, as CSI(Tl), and $\sim$11% more light ($\lambda_{max} = 420$ nm) than NaI(Tl), would be a considerably better match with the fiber optic coupled MC-PMT imaging system, and we believe it will be the crystal of choice in the final design.

An additional advantage of this approach is that the photodetector end, virtually all the cost of the system, can be used for both beta and gamma imaging. It allows a simple change between the beta and gamma imaging devices, as necessitated by the particular procedure, requiring only simple hardware and software changes. This study is an example of the application of high energy and nuclear physics techniques being adapted to a medical application.

Acknowledgements

This work was supported in part by DoE Contract DE-FC03-87-ER60615 and NCI grants R01-CA61037 and T32-CA09092.

References

[1] L.R. MacDonald et al., IEEE Trans. Nucl. Sci. NS-42 (1995) 1351.
[2] M.P. Tornai et al., J. Nucl. Med. 36 (1995) 109.
[3] L.R. MacDonald et al., Proc. SPIE: Photoelectronic Detectors, Cameras and Systems 2551 (1995) 92.
[4] C.S. Levin, L.R. MacDonald, M.P. Tornai, E.I. Hoffman and J. Park, IEEE Trans. Nucl. Sci. NS-43 (1996) 2053.
[5] M.P. Tornai, L.R. MacDonald, C.S. Levin, S. Siegel and E.J. Hoffman; IEEE Trans. Nucl. Sci. NS-43 (1996) 2326.
[6] M.P. Tornai, E.J. Hoffman, L.R. MacDonald and C.S. Levin, Proc. IEEE Nucl. Sci. Symp. & Med. Imag. Conf., San Francisco, CA, USA (1995) p. 1632; and IEEE Trans. Nucl. Sci. NS-43(1996) 3342.
[7] H.B. Barber, H.H. Barrett, W.J. Wild and J.M. Woolfenden, IEEE Trans. Nucl. Sci. NS-31 (1984) 599.
[8] N.E. Hartsough et al., Proc. SPIE: Catheter-Based Sensing and Imaging Technology, 1068 (1989) 92.
[9] B.E. Patt, J.S. Iwanczyk, M.P. Tornai, C.S. Levin and E.J. Hoffman in: Advances in X-ray Analysis, Vol. 38. ed. P. Predicki et al. (Plenum Press, New York, 1995) p. 615.
[10] B.E. Patt, J.S. Iwanczyk, M.P. Tornai, C.S. Levin and E.J. Hoffman, Nucl. Instr. and Meth. A 366(1995) 173.
[11] B.E. Patt et al., Nucl. Instr. and Meth. A 380 (1996) 295.
[12] Y. Shao, S.R. Cherry, S. Siegel and R.W. Silverman, IEEE Trans. Nucl. Sci. NS-43 (1996) 1938.
[13] G.F. Knoll, T.E. Knoll and T.M. Henderson, IEEE Trans. Nucl. Sci. NS-35 (1998) 872
[14] S. Siegel, R.W. Silverman, Y. Shao and S.R. Cherry, IEEE Trans. Nucl. Sci. NS-43 (1996) 1634.
[15] A.I. Bird, T.Carter., A.J. Dean, D. Ramsden and B.M. Swinyard, IEEE Trans. Nucl. Sci. NS-40 (1993) 395.
[16] S.R. Cherry, Y. Shao, M.P. Tornai, S. Siegel, A.R. Ricci and M.E. Phelps, IEEE Trans. Nucl. Sci. NS-42 (1995) 1058.
[17] M. Dahlbom and E.J. Hoffman, IEEE Trans. Med. Imag. M1-7 (1988) 264.